Discover Applied Sciences

RESEARCH

Open Access

Influence of heat treatment on the microstructure, microhardness, and machinability of cast and additive manufactured AlSi10Mg

Amith K. V.[1], Navneet Khanna[2], Raviraj Shetty[1], Sathish Rao U.[1], Gururaj Bolar[1*] and Ashwin Polishetty[3]

*Correspondence:
Gururaj Bolar
gururaj.bolar@manipal.edu
[1]Manipal Institute of Technology, Manipal Academy of Higher Education, Manipal, India
[2]Department of Mechanical and Aerospace Engineering, Institute of Infrastructure Technology, Research and Management, Ahmedabad, India
[3]School of Engineering, Computer and Mathematical Science, Auckland University of Technology, Auckland, New Zealand

Abstract

This study aims to evaluate how T6 heat treatment influences the microstructure and microhardness of both cast and additively manufactured (AM) AlSi10Mg. Furthermore, effect of microstructure and microhardness on the machinability of AlSi10Mg was assessed considering the chip morphology, cutting force, machining temperature, and surface roughness. Initially, untreated cast and AM AlSi10Mg exhibited distinctly different microstructures. T6 heat treatment caused substantial alterations in both the microstructure and microhardness of the materials. In both material variants, silicon (Si) experienced fragmentation, followed by spheroidization and subsequent coarsening. However, the heat-treated AM specimens exhibited finer and more uniformly spheroidized Si particles than their cast counterparts. The untreated AM AlSi10Mg showed substantially higher microhardness than the cast alloy. Upon heat treatment, the AM material experienced softening and reduced hardness, whereas the cast material exhibited a notable increase in hardness. Machining the untreated AM alloy generated higher machining temperatures and cutting forces relative to the cast alloy. Post heat treatment, the AM alloy decreased both cutting force and temperature, while the cast alloy exhibited an increase in both parameters. Surface finish was consistently superior in AM specimens compared to cast ones in untreated and heat-treated conditions. Chip morphology also varied significantly: longer chips were produced when milling cast specimens, whereas shorter chips were observed with the AM material. Heat treatment reduced chip size for the cast alloy, while chip morphology remained largely unchanged for the AM material.

Keywords AlSi10Mg, Additive manufacturing, Laser powder bed fusion, Heat treatment, Cleaner production

1 Introduction

Laser Powder Bed Fusion (LPBF) is a metal additive manufacturing (AM) technique that fabricates components layer by layer from metal powder, utilizing a laser beam as the heat source. The process offers greater freedom to design and fabricate parts with complex geometries, reducing processing time, carbon emissions, and material wastage [1]. It also enables the production of components with a superior strength-to-weight ratio, suitable for aerospace, biomedical, and automotive applications [2, 3]. The AM system can support various materials, including cobalt-chrome, stainless steel, nickel, aluminum, titanium, and copper alloys. Aluminum alloys are extensively utilized across various industrial applications, with the Aluminum-Silicon (Al–Si) system being particularly common, known for its favorable specific strength and corrosion resistance [4, 5]. Among Al–Si alloys, AlSi10Mg is commonly used and produced through both AM and casting methods.

The material structure of AM AlSi10Mg is significantly different than the cast AlSi10Mg. AM of AlSi10Mg results in an ultrafine microstructure characterized by Al matrix encased in a network of Si particles, resulting from the rapid ejection and solidification of Si under high cooling rates (10^3–10^6 °C/s) [6–8]. Additionally, dense networks of entangled dislocations are present within Al matrix, formed because of rapid solidification conditions [9]. When subsequent layer melting induces sufficient reheating, it can promote diffusion, promoting the formation of Mg_2Si precipitates and Si dispersoids [7, 10]. The mechanical properties of printed AlSi10Mg are greatly influenced by these microstructural characteristics [11, 12].

One of the main process-related challenges faced by additively manufactured (AM) aluminum alloys is their structural anisotropy, which significantly hinders their use in conventional engineering applications that require properties to be uniform and isotropic [13, 14]. While the refined microstructure of AM material significantly enhances hardness and tensile strength, it simultaneously introduces limitations such as reduced ductility, higher brittleness, and increased residual stresses, which may adversely impact fatigue performance and fracture toughness [15, 16]. Furthermore, poor surface finish and limited dimensional accuracy restrict the direct use of AM parts in industrial settings. Therefore, post-processing operations, including machining and heat treatment, are crucial to overcome these drawbacks and ensure the parts meet application requirements.

Heat treatment plays a crucial role in influencing the microstructure and mechanical properties of AM AlSi10Mg. The commonly used heat treatment methods for AlSi10Mg are T5, T6, and annealing, each offering unique benefits in reducing residual stresses and modifying the microstructure and mechanical properties. Among these, T6 heat treatment, which involves solution treatment, quenching, and artificial aging, is particularly notable for optimizing the strength-ductility balance in AlSi10Mg alloys [17]. T6 heat treatment has been reported to relieve residual stresses while substantially decreasing material anisotropy [18]. During solution treatment, the fine cellular α-Aluminum (α-Al) structure in SLM-processed AlSi10Mg dissolves partially, resulting in the redistribution of Si particles and a temporary decline in hardness [19, 20]. This microstructural change allows for the relaxation of residual stresses and enhances ductility by reducing grain boundary-strengthening effects [21]. Subsequent quenching aids in suppressing premature precipitation, while the artificial aging process facilitates the precipitation of strengthening phases, thereby increasing hardness and restoring mechanical strength via. precipitation hardening [22, 23]. AlSi10Mg was subjected only to artificial aging and was found to retain its original microstructure [24]. However, prolonged aging or exposure to high temperatures can induce over-aging, causing the coalescence of precipitates and subsequent reduction in hardness and strength [17, 19, 20]. Also, it the case of Al-Si alloys, besides Ostwald's dissolution, the growth of Si particles can also result from impingement, fusion, and agglomeration. Higher Si content makes achieving spheroidization more challenging due to fragmentation and coarsening [25]. The direct aging method successfully increased microhardness, while the T6 heat treatment caused a reduction in microhardness. Additionally, the direct aging treatment enhanced the ultimate tensile strength, unlike the T6 heat treatment, which resulted in a decrease in strength [26]. T6 heat treatment can markedly improve fatigue performance of AM alloy [27]. The dendritic eutectic Si networks present in AlSi10Mg alloys enhanced the hardness and impact toughness of AlSi10Mg [28, 29]. Additionally, solution treatment at 550 °C followed by aging at 180 °C produced the best overall property enhancement [6]. Surface preheating also affected the microstructure and mechanical characteristics of the AlSi10Mg alloy. Preheating led to the coarsening of nano-sized Si precipitates and a decrease in solid solution strengthening. Additionally, there was fragmentation of the continuous eutectic Si. These microstructural alterations resulted in a reduction of both the ultimate tensile strength and yield strength of the material [30].

Machining serves as a post-processing technique to improve the dimensional accuracy and surface finish of AM components. Research indicates that the machining characteristics of AM AlSi10Mg differ considerably from those of its cast counterpart. Due to its refined cellular dendritic microstructure, AM AlSi10Mg typically encounters higher cutting forces and results in inferior surface quality under comparable cutting conditions [31]. This microstructure also leads to increased hardness, which aids in minimizing burr formation during milling [31]. Additionally, microstructural features influence chip morphology. AM AlSi10Mg generally produces shorter chips compared to the cast alloy because its greater porosity and brittleness promote microcrack formation and enhance chip fragmentation [32]. The microstructure and microhardness also influenced the specific cutting energy (SCE). A higher SCE with increased vibration was noted when milling AM A205 aluminum alloy than the cast counterpart. However, a superior surface finish was observed while milling AM components due to finer grain structure and higher microhardness [33]. Heat treatment also affects machinability. Solution-treated AM aluminum alloys, due to their increased ductility, often exhibit poorer surface quality, heightened vibrations, and increased SCE during machining [34]. Researchers have suggested several strategies to overcome the milling challenges of AM AlSi10Mg. The down-milling technique resulted in a superior surface finish compared to traditional milling methods [32]. Additionally, using Minimum Quantity Lubrication (MQL) reduced flank wear and surface roughness more effectively than dry cutting [35]. Moreover, employing vegetable oils with MQL enhanced milling performance by lowering cutting temperatures and reducing tool wear, thus achieving better surface characteristics [36]. Cryogenic cooling has also been shown to be an effective method, significantly minimizing tool wear and surpassing dry, flood, and MQL-based techniques [37].

The literature review highlights the need for heat treatment operations to mitigate the detrimental effects of the AM process. Moreover, post-processing through machining is crucial for improving surface characteristics of AM parts. As reported, AM alloys exhibit distinct mechanical and microstructural characteristics compared to their conventionally produced counterparts, significantly affecting their machinability. However, despite extensive research on heat treatment of AM AlSi10Mg, influence of microstructure on machinability is yet to be thoroughly investigated. Moreover, machinability comparison between heat-treated cast and AM AlSi10Mg has not been adequately covered by previous research. This study aims to address the existing knowledge gap by examining how heat treatment affects the microhardness and microstructure of both cast and AM AlSi10Mg. Additionally, the machinability of cast and AM aluminum alloy is evaluated under untreated (as-fabricated) and heat-treated states, considering cutting forces, surface roughness, machining temperature, and chip morphology.

2 Materials and methods

AlSi10Mg alloy specimens were fabricated using casting and AM routes. The AM parts were produced using a LPBF system (EOS M280) with an Argon atmosphere. The feedstock consists of gas-atomized AlSi10Mg powders, averaging between 15 and 50 µm in particle size. The material was fabricated using a laser source with a 370 W power setting, 1300 mm/s scan speed, 0.19 mm hatch spacing, and a 30 µm layer thickness. A stripe scanning strategy with 67° inter-layer rotation and a 7 mm stripe width was used. The cast AlSi10Mg alloy was prepared using commercially aluminum ingots. Si and Magnesium (Mg) were added in the form of Al–Si and Al–Mg master alloys, respectively. The cast AlSi10Mg specimens were produced by melting the materials in a steel crucible at 740 °C for four hours, followed by casting in a steel mold preheated to 710 °C. After cooling, the ingots were sectioned to the required dimensions using the Wire Electrical Discharge Machining process. The density of the cast and AM AlSi10Mg specimens was measured using liquid displacement method. To ensure accuracy and repeatability, several measurements were carried out, and the average density value is recorded. Accordingly, the density of AlSi10Mg produced through LPBF is 2.68 g/cm^3, while the density of its as-cast version is 2.77 g/cm^3. Table 1 provides specifics about the chemical composition for the cast specimen and the AlSi10Mg powders as provided by the supplier.

A muffle furnace was employed to heat-treat the cast and printed specimens. The heat treatment cycle followed is shown in Fig. 1.

Milling experiments were conducted on a vertical machining center (VMC) (AMS Spark). Figures 2(a, b) illustrate the experimental setup, which includes the custom fixture and one of the cutting tools. Two fluted end mills were employed during the study, as they help in easier chip evaluation and prevents chip clogging, which is crucial when working with aluminum alloys. The machining tests involved four types of specimens: as-built (AM), as-cast, T6 heat-treated AM, and cast AlSi10Mg alloys. End mills were coated with amorphous tetrahedral carbon (ta-C) through PVD-arc deposition (Oerlikon Balzers), which is recognized for its high hardness (50–60 GPa), and low friction coefficient (0.1–0.2), offering superior tribological characteristics and resistance to wear. Selected end mills had two flutes, 35° helix angle, a flute length of 18 mm. Dry machining, a sustainable method of metal cutting was employed for all the trials. The milling trials were conducted by varying the cutting speed at two levels (25, 75 m·min^{-1}), and cutting feed at two levels (0.06, 0.18 mm·rev^{-1}). The level of cutting speed was selected considering the limitations of the machine tool. Since the study focused on evaluating only the cutting forces, surface roughness and machining temperature, lower feeds were employed to limit the adverse effect of tool wear. The axial and radial cut depth were

Table 1 AlSi10Mg alloy chemical composition

Material	Elements	Si	Mg	Mn	Cu	Fe	Ni	Zn	Sn	Ti	Pb	Al
AM	Wt%	10.0	0.4	0.4	0.05	0.5	0.05	0.1	0.05	0.15	0.05	Bal
Cast	Wt%	10.7	0.45	0.3	0.03	0.3	-	-	-	0.18	-	Bal

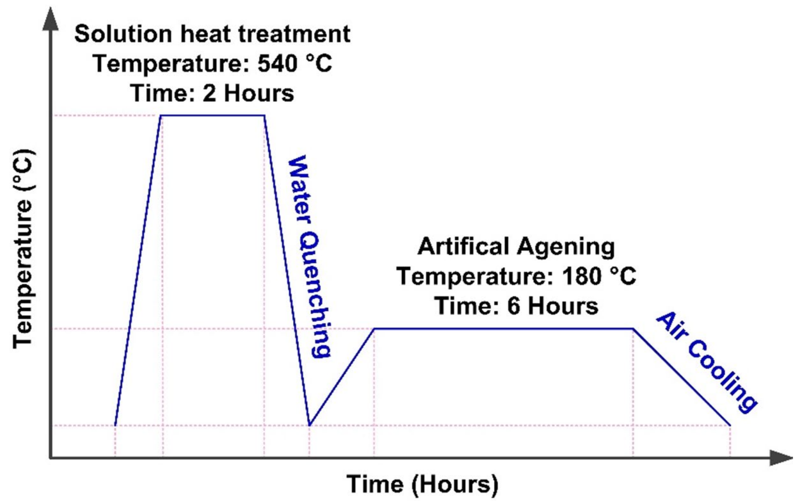

Fig. 1 T6 heat treatment cycle employed

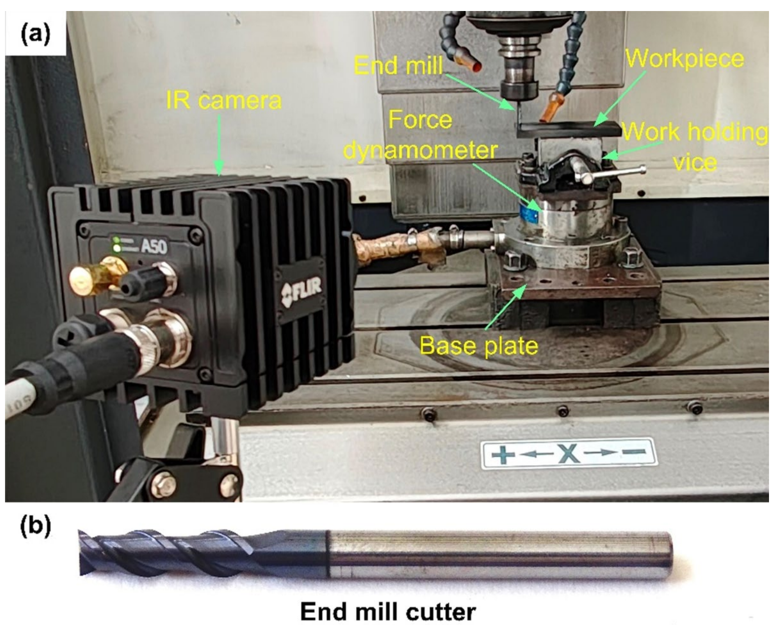

Fig. 2 (**a**) Experimental setup with fixture, (**b**) Cutting tool employed in the machining experiments

maintained at 1 mm and 5 mm, respectively. To ensure consistency and reliability of the results, each set of machining conditions was repeated three times.

Machined surface morphology, chips and microstructure were characterized using the optical microscope (Olympus BX53M). Additionally, a scanning electron microscope (SEM) (Zeiss EVO 18) was utilized to examine the chips and the microstructure of the material. An energy-dispersive spectroscopy (EDS) detector (Oxford) was employed to analyze elemental composition. Specimens were treated with Keller's reagent following guidelines of ASTM E407. X-ray diffraction (XRD) analysis was conducted using X-ray diffractometer (Rigaku Miniflex 600) equipped with a copper tube operating at 40 kV and 15 mA. The measured 2θ diffraction angle ranged from 20° to 80°, with increments of 0.5°. Vickers microhardness measurements were performed using a Matsuzawa

MMT-X tester with a diamond pyramid indenter, applying a 200 g load for 15 s per indentation, in accordance with the ASTM E92 standard. To ensure statistical reliability, ten readings were obtained from random locations of the cast and AM specimens. The microhardness values presented are the average of these measurements. The associated error was calculated as the standard deviation of the dataset.

An infrared (IR) camera (FLIR A50), with an operating range of -20–1000 °C, was used to capture the machining temperature. The emissivity setting was adjusted to 0.95 to ensure accurate temperature readings. The machined surfaces were assessed for surface roughness using non-contact profilometer (Contour–Bruker), with arithmetic mean height (Sa) serving as the roughness indicator. A dynamometer (Kistler 9272) linked to charge amplifier (Kistler 5070 A) was employed to measure and obtain three force components at 4000 Hz. Dynoware software was utilized to examine force signals. Resultant cutting force was derived from the three orthogonal components (Fx, Fy, Fz) using Eq. 1 [38].

$$F = \sqrt{F_x^2 + F_y^2 + F_z^2} \tag{1}$$

3 Results and discussion

3.1 XRD analysis

Figure 3 illustrates the XRD diffraction patterns for both the cast and AM AlSi10Mg alloy, observed before and after undergoing heat treatment. By utilizing the International Centre for Diffraction Data (ICDD) patterns 01-089-2837 and 01-089-5012, the primary peaks associated with Al and Si were identified. The XRD diffraction patterns for the as-cast and as-built samples reveal low-intensity peaks for Si (111), Si (220), Si (311), Si (400), and Si (331), with these peaks being more prominent in the AM specimen. Strong diffraction peaks for aluminum, specifically Al (111), Al (200), Al (220), and Al (311), were noted, with greater intensity in the as-built AM material. Furthermore, the Mg_2Si phase was detected, aligning with ICDD pattern 00-001-1192, confirming a

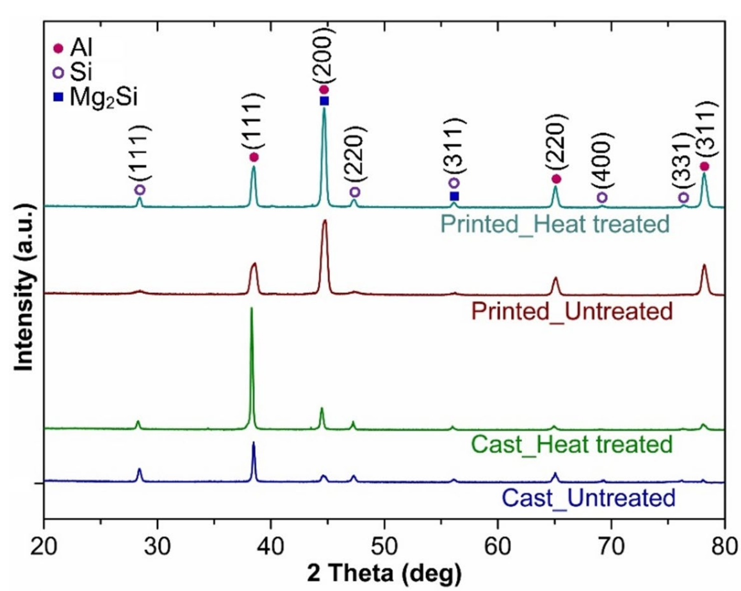

Fig. 3 XRD pattern of cast and AM AlSi10Mg alloy before and after heat treatment

chemical interaction between Mg and Si. However, the diffraction intensity of the Mg_2Si phase was quite low, indicating its minimal presence in both the as-cast and as-built specimens.

Figure 3 also illustrates the XRD patterns for both the cast and AM materials after undergoing heat treatment. Post heat treatment, there was an increase in the intensity of the Si peak compared to the untreated samples. This enhancement in the Si phase diffraction peak after heat treatment is mainly due to the precipitation of Si from the α-Al matrix in the AlSi10Mg alloy [11]. This indicates a significant decrease in the solubility of Si within the Al matrix after the heat treatments [11, 39]. Additionally, for the AM AlSi10Mg, the Si-rich cellular boundaries transformed into distinct Si particles along the α-Al matrix boundaries, with these Si particles enlarging during solution treatment, thereby increasing the peak intensity [5, 6]. The XRD pattern of the AlSi10Mg specimen subjected to T6 heat treatment showed Mg_2Si peaks with a significant increase in intensity, especially in the AM material. This heightened intensity is due to the precipitation of Si from the supersaturated α-Al matrix during the heat treatment, followed by the reaction of the separated Si with Mg to form the Mg_2Si phase [11, 40].

3.2 Microstructural analysis

Figure 4(a, b) illustrates the microstructure of AlSi10Mg alloy in its as-cast state. It features dendritic primary α-Al along with a lamellar eutectic structure made up of α-Al and Si. In an as-cast specimen, a slow cooling rate results in Si solid solution breakdowns within Al-matrix, forming coarser plate-like Si precipitates. The matrix contains the primary α-Al phase, which is enveloped by a continuous eutectic network composed of Al and Si. The SEM image shows the presence of needle-like Si, a characteristic attributed to the hypoeutectic composition. Figure 4(c) presents an area-scan EDS spectrum illustrating the presence of Al, Si, Fe, Mn, and Mg in the chosen region. This analysis offers only qualitative elemental data and does not enable the conclusive identification of

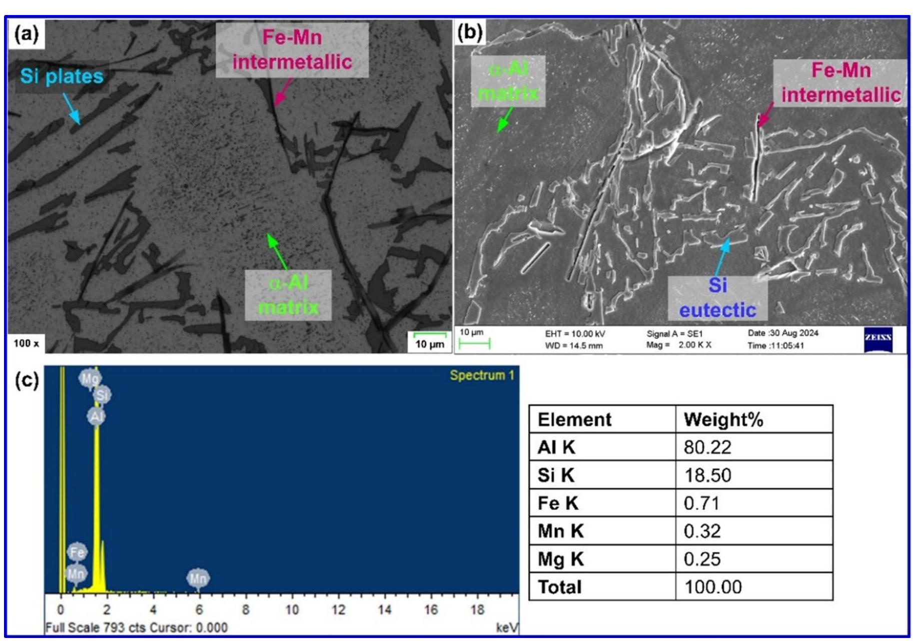

Fig. 4 (**a**) Optical microscopy-based microstructure of as-cast AlSi10Mg alloy, (**b**) SEM image of as-cast AlSi10Mg alloy microstructure (**c**) Area-EDS elemental spectra and composition

specific intermetallic phases like Mg_2Si. However, the XRD pattern shown in Fig. 3 suggests the potential presence of the Mg_2Si phase, as indicated by the appearance of faint peaks. This implies that the Mg_2Si phase is present in minimal amounts in the as-cast specimens.

Figure 5(a, b) presents the microstructure of the AM specimen obtained using optical microscopy. The microstructure widely differs from the as-cast material. These micrographs show the presence of solidified melt pools, with adequate overlap and densification along the build and scan directions. Figure 5(a) illustrates distinct scanning patterns on the XY-plane with widths ranging from approximately 100 to 200 µm and with varying lengths. The XY-plane exhibits scan path patterns oriented at an angle of 67°. Melt pools are visible in the build direction (Z plane), displaying their semi-circular morphology (see Fig. 5(b)). The overlapping melt pools depict the paths traced by the scanning laser, with the arrow denoting the build direction. This arrangement resembles the pattern of fish scales, where each scale corresponds to an individual melt pool.

The SEM images of the as-built specimen indicate fine cellular dendritic structure formation, as illustrated in Fig. 6. A fibrous network of eutectic Si characterizes the cell walls. In metals that solidify under conditions of rapid cooling and low solute levels, a cellular dendritic structure often emerges. For Al-Si alloys, higher cooling rates during LPBF can enhance the solubility of Si within the aluminum matrix. The LPBF process, characterized by extremely high cooling rates (10^3–10^6 °C/s), promotes greater Si solubility in Al-matrix [6–8]. This rapid solidification also minimizes constitutional undercooling by decreasing the Si concentration in the liquid phase. Consequently, accelerated cooling and solidification in the LPBF process led to cellular dendritic structure formation in the untreated AM alloy.

Further examination of the printed specimen along the scan direction (XY-plane) illustrates the presence of overlapping melt pools consisting of three distinct zones (see Fig. 7(a). These consist of a fine cellular zone (FCZ) with fine grains located within melt pool, a coarser cellular zone (CCZ) featuring a coarser grain structure positioned a few microns from the melt pool boundary, and heat-affected zone (HAZ) surrounding the melt pool in adjacent melt pools. HAZ forms due to elevated temperatures generated by laser heating and the creation of neighbouring melt pools. This disrupts the close cellular network within the HAZ, leading to the coarsening observed within the intercellular phase. The borders of the melt pool experience multiple cycles of melting and solidification, which results in a coarser microstructure compared to the finer morphology

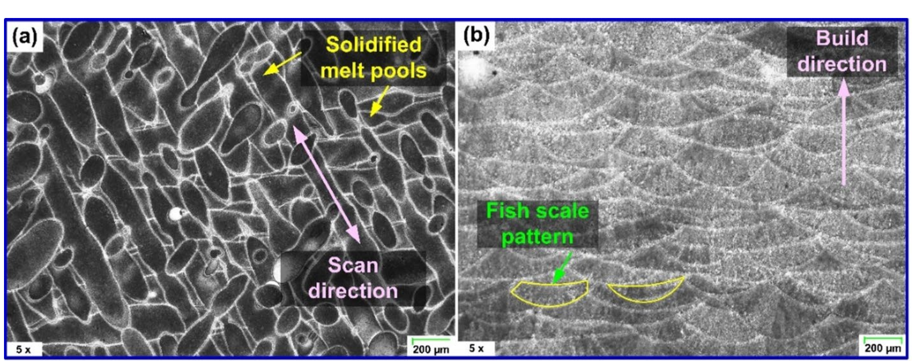

Fig. 5 Optical micrograph of as-built AlSi10Mg alloy (**a**) Along scan direction (XY-plane), (**b**) Along build direction (Z-direction)

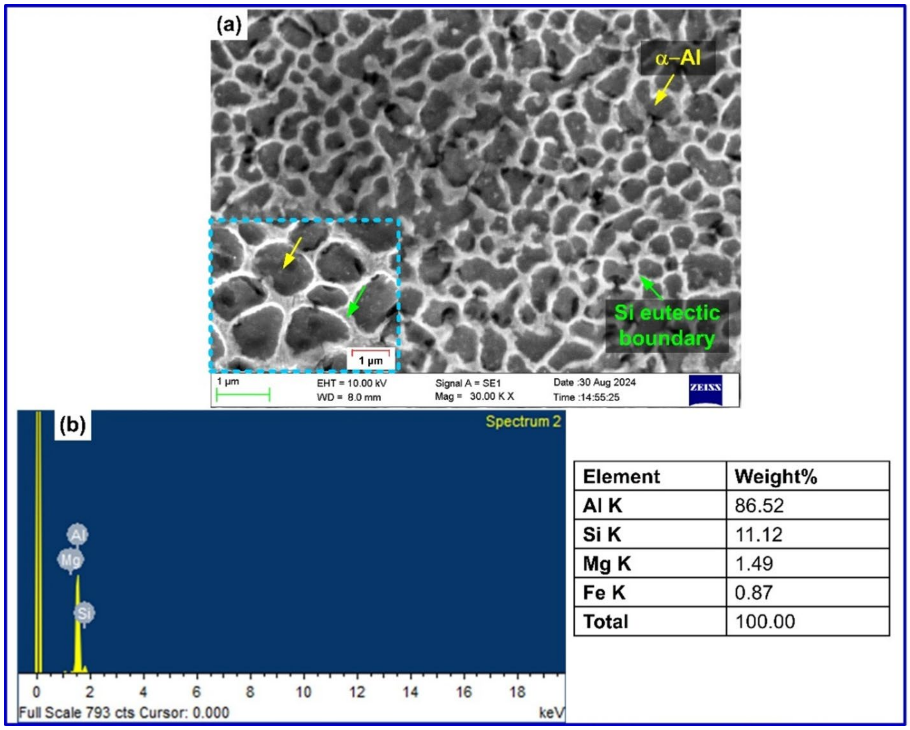

Element	Weight%
Al K	86.52
Si K	11.12
Mg K	1.49
Fe K	0.87
Total	100.00

Fig. 6 (**a**) SEM of as-built AlSi10Mg alloy microstructure, (**b**) Area-EDS elemental spectra and composition

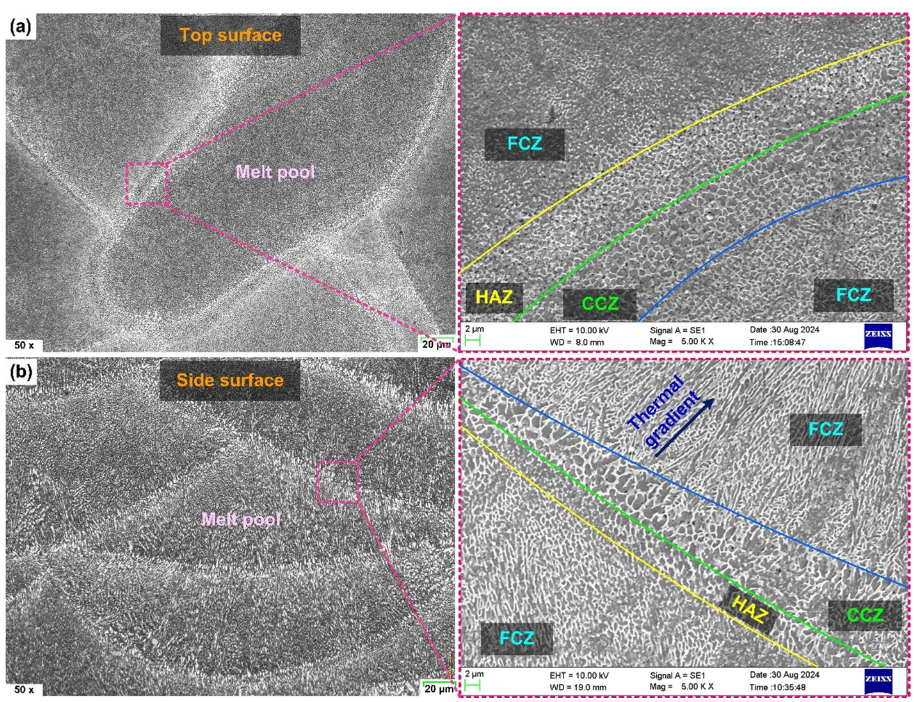

Fig. 7 Microstructure of as-built AlSi10Mg alloy along (**a**) Scan direction (XY-plane), (**b**) Build direction (Z-plane)

observed at the center of melt pools. The variation in microstructure observed is due to overlapping of laser scans and the layer-by-layer solidification characteristic of the process, which results in different thermal histories from center to the edge of the melt pool [41]. Importantly, solidification rate (R) and temperature gradient (G) are crucial parameters that significantly affect the microstructure of a given alloy composition. These parameters change throughout melt pool, from its center to its edges. At the center, where temperature gradient is highest and solidification rate is lowest, a fine cellular-dendritic structure tends to form. Conversely, at the boundaries of the melt pool, a decrease in temperature gradient and an increase in the solidification rate result in the formation of a more elongated and coarser dendritic structure [42].

Figure 7(b) presents the surface morphology and microstructure of as-built specimen along the build direction (Z-plane). In line with the top surface, the building-direction's overlapping melt pools also indicate the presence of three zones, including the FCZ, CCZ, and HAZ. In addition, the side view microstructure shows characteristics of non-equilibrium directional solidification, indicative of epitaxial growth directed towards the subsequent layer. This growth pattern is oriented towards the melt pool center, as seen in the micrograph.

In cast alloys, heat treatment effectively alters the shape of the acicular eutectic Si lamellae, turning them into more spherical particles. Initially, the Al matrix shows an uneven distribution of Si, marked by elongated, needle-like eutectic Si particles. When subjected to solution treatment at 540 °C, these particles undergo significant morphological changes as described by Lifshitz–Slyozov–Wagner (LSW) theory. This transformation is driven by diffusion-controlled Ostwald ripening, where the fine, plate like Si lamellae, having a higher chemical potential, dissolve, while solute diffuses through the α-Al matrix and re-precipitates onto larger particles. This thermodynamically driven reduction in interfacial energy results in particle coarsening, rounding, and spheroidization. The kinetics of this transformation adhere to the LSW coarsening law, confirming diffusion-controlled growth and resulting in the breakdown of the acicular structure into distinct, spheroidized Si particles, as illustrated in Fig. 8.

Subsequent quenching suppresses premature precipitation by retaining solute atoms in a supersaturated solid solution. However, during artificial aging, enhanced diffusion

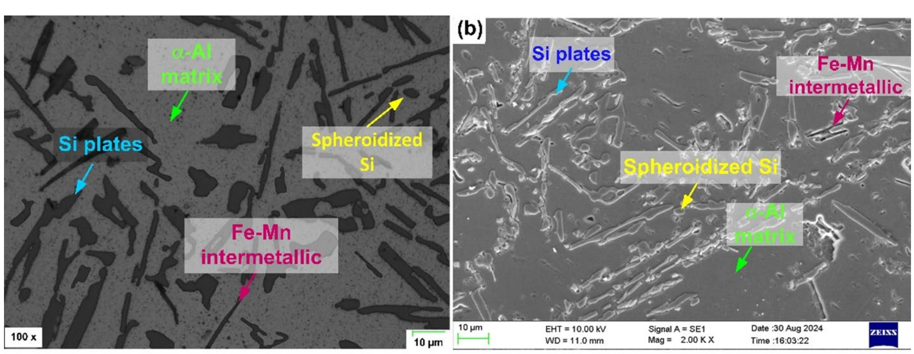

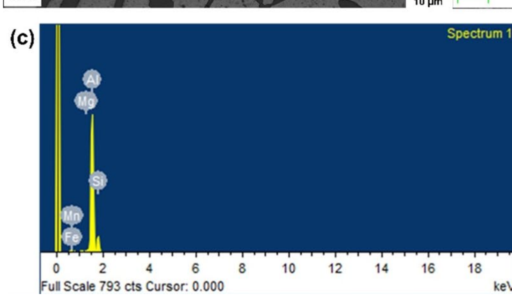

Element	Weight%
Al K	80.49
Si K	16.99
Fe K	0.88
Mn K	1.16
Mg K	0.48
Total	100.00

Fig. 8 (**a**) Optical micrograph of heat-treated cast AlSi10Mg alloy, (**b**) SEM image of heat-treated cast AlSi10Mg, (**c**) Area-EDS elemental spectra and composition

facilitates microstructural stabilization and refinement of the Si phase distribution [43]. In the present study, solutionizing heat treatment and aging duration were kept at 540 °C for 2 h. As a result, only partial spheroidization of the acicular Si particles is observed, indicating a need for longer heat treatment duration to visualize complete spheroidization of Si particles. Additionally, because intermetallic phases such as Mg_2Si and needle-like Fe-rich phases exhibit significant thermal stability, heat treatment has little to no impact on them.

The microstructure of AM AlSi10Mg that has undergone heat treatment exhibits significant differences when compared to the specimen in its as-built state. Specifically, the interconnected, fibrous coral-like Si particles transformed into spherical Si particles, distributed uniformly throughout the Al-matrix, exhibiting varied shapes and sizes. Due to an excessive amount of Si, supersaturated α-Al is thermodynamically unstable. Consequently, during solutionizing, surplus Si atoms dissolved in the α-Al matrix are inclined to be expelled from the matrix, leading to the formation of fine Si particles distributed throughout the α-Al-matrix. Microstructure appears homogeneous, with no significant differences noted along longitudinal and transverse cross-sections. Notably, inter-cellular network, laser traces, and HAZ have become indistinguishable, as the columnar and "fish-scale" features disappear mainly due to coarsening of Si particles amid heat treatment. Figure 9 also shows that the microstructure consists of both coarse and fine spheroidized Si particles. This phenomenon occurs because the coarse particles originate from the Si-rich network at the boundaries of α-Al cells, while the fine particles form from fine precipitates [44]. Closer inspection reveals that during solidification, Fe-rich needle-like intermetallic phases manifest as particles with an elongated form.

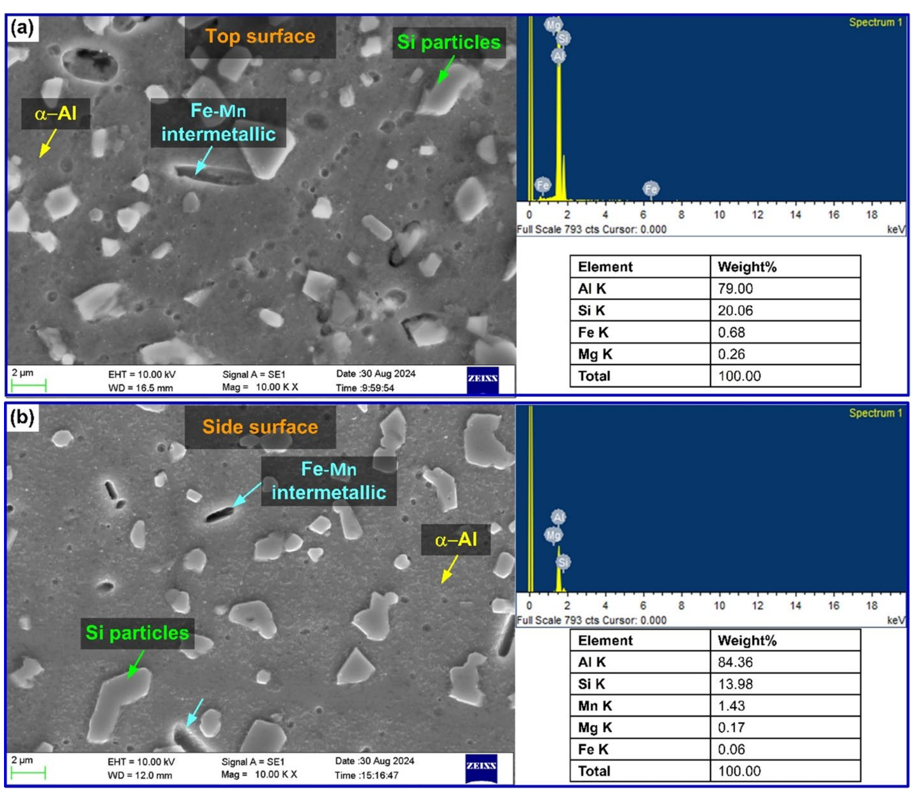

Fig. 9 Microstructure of T6 heat-treated AM AlSi10Mg with EDS elemental spectra and composition in the (**a**) Scan direction (XY-plane), (**b**) Build direction (Z-plane)

Overall, it is noted that the morphological evolution of eutectic Si via., fragmentation, spheroidization, and coarsening are time- and temperature-dependent mechanisms. Hence further studies are necessary to fully explore these phenomena.

3.3 Analysis of microhardness

Figure 10 presents the average microhardness of as cast and heat-treated AlSi10Mg. An average microhardness value of 74–75 HV is measured for the as-cast alloy. Post-heat treatment, microhardness of as-cast specimen increases significantly to around 125–127 HV. This represents a substantial 73% increase in hardness after heat treatment. Moreover, hardness values for a as-cast specimen exhibit no significant variation between the top face (X-Y) and side face (Z) due to the uniform microstructure typically achieved through the casting process. Due to the consistent cooling rates and solidification patterns, the as-cast alloy shows a homogeneous distribution of phase constituents and grain structure. The absence of mechanical anisotropy in cast specimens leads to an even distribution of hardness irrespective of the measurement orientation. With the T6 heat treatment, several critical microstructural transformations occur in cast AlSi10Mg alloys. During the solutionizing step, the alloy experiences grain coarsening, fragmentation, and spheroidization of eutectic Si and dissolution of excess Si into the Al-matrix. The primary refinement of the microstructure is due to the alteration and redistribution of eutectic silicon [5, 11]. The subsequent quenching process rapidly cools the alloy, trapping supersaturated solid solution and retaining a high concentration of dissolved elements. In the artificial aging stage, controlled precipitation of finely distributed particles enhances the hardness by inhibiting dislocation movement and refining the microstructure. The Mg based intermetallic particles precipitate in a controlled manner, which increases hardness and strength by hindering dislocation movement through precipitation strengthening [11, 45]. Intermetallic phases containing Fe and Mn remain mostly stable during heat treatment and serve as rigid barriers to plastic deformation [46].

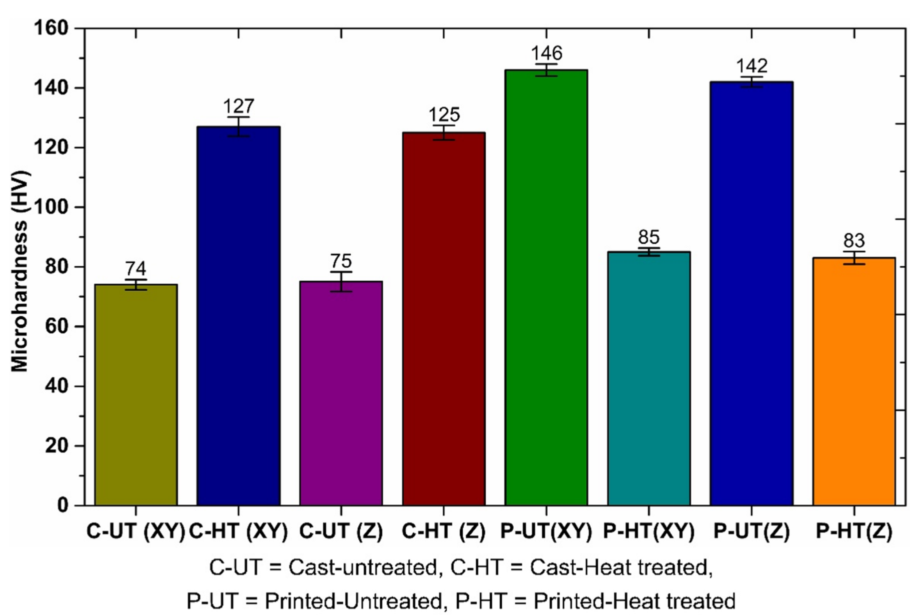

Fig. 10 Average microhardness values for untreated and heat-treated cast and AM AlSi10Mg

Furthermore, the AM specimens clearly demonstrate higher hardness compared to the cast counterparts. The fast solidification and high cooling rates of AM process (10^3–10^6 °C/s) are largely responsible for the finer grain structure and uniform dispersion of eutectic Si within a supersaturated α-Al matrix, resulting in increased hardness [6–8]. Furthermore, Si enhanced solubility in α-Al matrix contributes to solid solution strengthening, which hinders dislocation movement. According to the Hall-Petch relationship, a smaller grain size increases the material's overall hardness by further preventing dislocation motion [7, 19].

In contrast to as-built specimen, the average microhardness on the AM part measured along the XY-plane decreases from 146 HV to 85 HV after heat treatment, indicating a 73% reduction in microhardness following heat treatment. Similarly, after heat treatment, the average microhardness measured along build (Z) direction decreases from 142 HV to 83 HV, indicating a 71% reduction. This decrease is accompanied by a more uniform microhardness distribution across the printed specimen, mainly resulting from changes in morphology of eutectic Si particles. Heat treatment breaks down the finer cellular structure typical of the as-built material as a result of thermal diffusion. Excess Si dissolved in Al-matrix begins to precipitate out, diminishing solid solution strengthening effect [18]. Additionally, the eutectic Si undergoes morphological transformation, where its initial cellular structure fragments and becomes more spherical (spheroidization), and coarsens into larger particles. Ultimately, the dislocation networks that develop during the rapid solidification phase of the AM process are destroyed, contributing to a reduction in hardness.

3.4 Machinability analysis

3.4.1 Cutting force

Figure 11(a, b) illustrates the cutting forces measured during milling of both cast and AM AlSi10Mg, in untreated and heat-treated conditions. Cutting force consistently decreases with increasing cutting speed in all four material states. This trend is attributed to the adiabatic nature of high-speed cutting, where limited heat dissipation raises the cutting zone temperature. The resulting thermal softening reduces material strength, lowering cutting resistance and thus the cutting force [48]. Conversely, cutting force increases with cutting feed across all samples. With constant cutting speed and cut depth, a higher cutting feed increases chip thickness, requiring greater energy to shear more material, thereby raising cutting forces [31, 48].

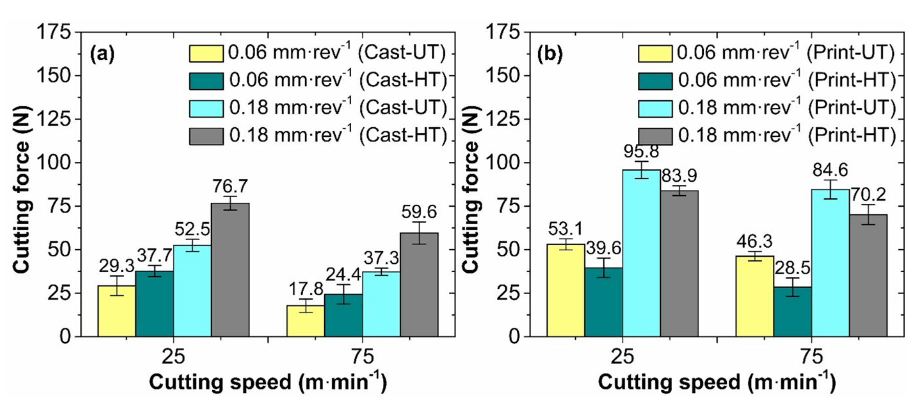

Fig. 11 Cutting force variation for untreated and heat-treated (**a**) Cast alloy, (**b**) Printed alloy

Notably, the cutting force required for milling the as-built AM AlSi10Mg is between 81% and 160% greater than that needed for its as-cast version. This phenomenon is attributed to finer, anisotropic cellular-dendritic microstructure that develops during the rapid solidification process in AM. High cooling rates increase silicon solubility in the α-Al matrix and promote grain refinement, which enhances microhardness (146 ~ 149 HV) through Hall–Petch strengthening. This microstructure resists plastic deformation, necessitating increased cutting forces because of dislocation accumulation and localized strengthening. In contrast, the as-cast AlSi10Mg, with its coarser microstructure and lower hardness, exhibits reduced cutting forces. Since the cooling rate during casting is slower, it leads to the development of course Si precipitates and a matrix mainly consisting of α-Al and eutectic Al-Si. This composition offers reduced resistance to deformation and makes material removal easier.

Heat treatment also significantly influences cutting force. Following T6 heat treatment, cutting force during milling of cast AlSi10Mg increases by approximately 28–60%. This rise is attributed to spheroidization of acicular Si particles and the formation of Fe- and Mn-rich intermetallic compounds, which collectively enhance the alloy's hardness after heat treatment. The homogenized microstructure of heat-treated AlSi10Mg, along with the Mg_2Si precipitates, acts as a barrier to plastic deformation, increasing the microhardness and yield strength of the cast material [21, 49]. As a result, more energy is required to shear the material, leading to an increase in cutting force. Conversely, with the T6 treatment, cutting force reduces by 14 ~ 62% when milling the AM AlSi10Mg specimen. Heat treatment transforms the interconnected, fibrous, coral-like Si particles into spherical ones uniformly distributed throughout the Al-matrix, thereby reducing dislocation pile-up at grain boundaries. Moreover, subjecting the AM material to heat treatment induces microstructural changes, that enhances the ductility by reducing grain boundary-strengthening effects [18, 21]. Consequently, this leads to a decrease in cutting resistance, which in turn reduces the cutting force required. Additionally, it is observed that even after heat treatment, milling AM AlSi10Mg generates higher cutting forces compared to the cast counterpart, indicating a greater energy requirement for machining the AM material.

3.4.2 Machining temperature

Figures 12, 13, 14 and 15 present the temperature maps illustrating how cutting parameters influence the machining temperatures in both cast and AM AlSi10Mg specimens, whether untreated or heat-treated. Generally, an increase in cutting speed and cutting feed leads to higher machining temperatures in all specimens. Rise in temperature at elevated cutting speeds is primarily due to a higher deformation rate and reduced cutting time. Increased spindle speed intensifies the rate of plastic deformation, resulting in greater heat generation at the cutting interface [50]. Moreover, increased speeds shorten the time the tool is in contact with workpiece, limiting heat dissipation and causing more heat to accumulate in workpiece, further elevating the temperature. A similar trend is noted with increasing feed rates, where the machining temperature rises consistently. This is attributed to the increased uncut chip thickness, which enhances plastic deformation and heat production. Additionally, higher feed rates intensify the friction between the chip and tool's rake face, resulting in more heat accumulation in the cutting

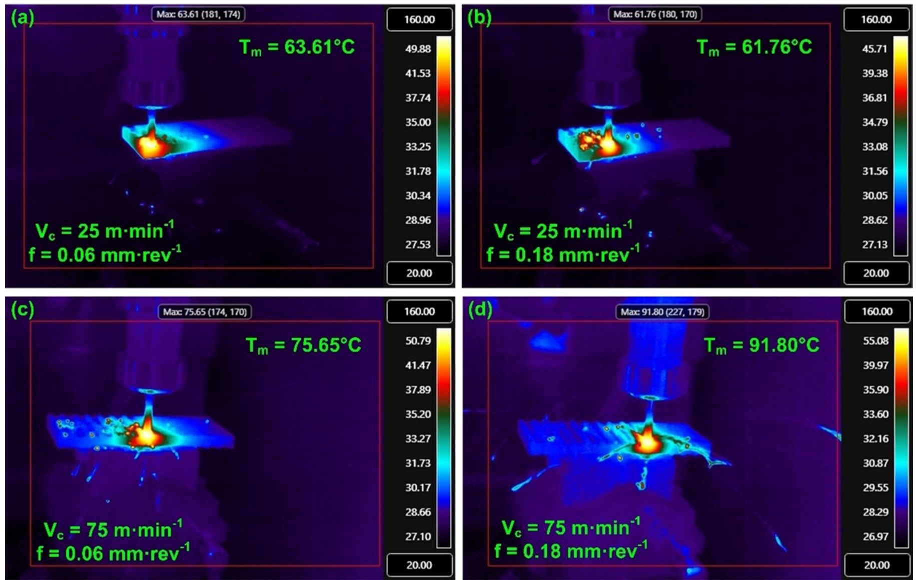

Fig. 12 Cartographies of temperature obtained while milling cast AlSi10Mg at a cutting speed and feed of (**a**) 25 m·min^{-1} and 0.06 mm·rev^{-1}, (**b**) 25 m·min^{-1} and 0.18 mm·rev^{-1}, (**c**) 75 m·min^{-1} and 0.06 mm·rev^{-1}, (**d**) 75 m·min^{-1} and 0.18 mm·rev^{-1}

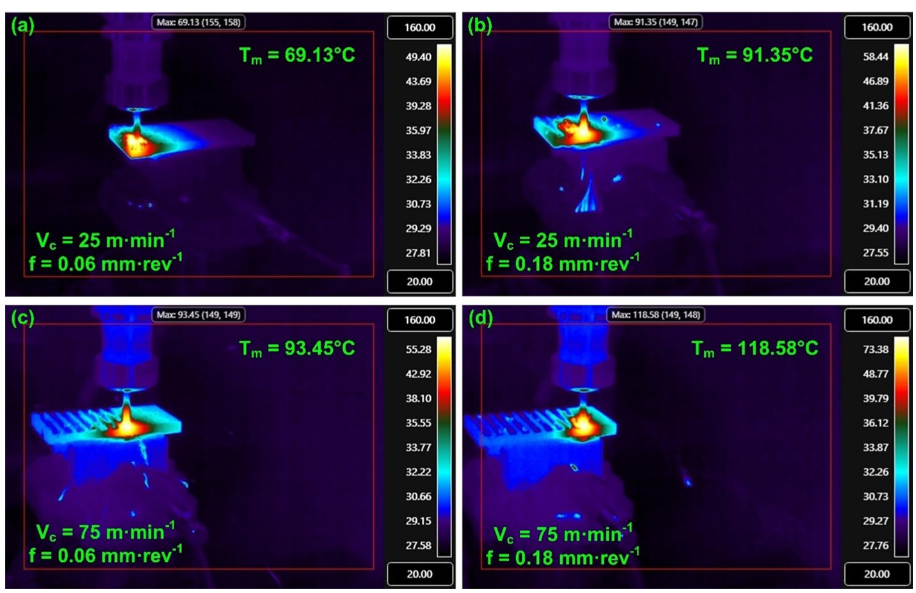

Fig. 13 Cartographies of the temperature obtained while milling AM AlSi10Mg at a cutting speed and feed of (**a**) 25 m·min^{-1} and 0.06 mm·rev^{-1}, (**b**) 25 m·min^{-1} and 0.18 mm·rev^{-1}, (**c**) 75 m·min^{-1} and 0.06 mm·rev^{-1}, (**d**) 75 m·min^{-1} and 0.18 mm·rev^{-1}

area [51]. These factors together lead to a gradual increase in machining temperature as cutting speed and feed rate rise.

Furthermore, the material processing route and the heat treatment are found to influence the machining temperature. The maximum machining temperature generated while milling the as-cast AlSi10Mg is found to be 9 ~ 48% lower than the as-built AlSi10Mg. It can be noted that the maximum machining temperatures are measured while machining the as-built AlSi10Mg. Elevated machining temperature observed in the as-built AlSi10Mg is once again linked to its microstructure and microhardness. Ultrafine

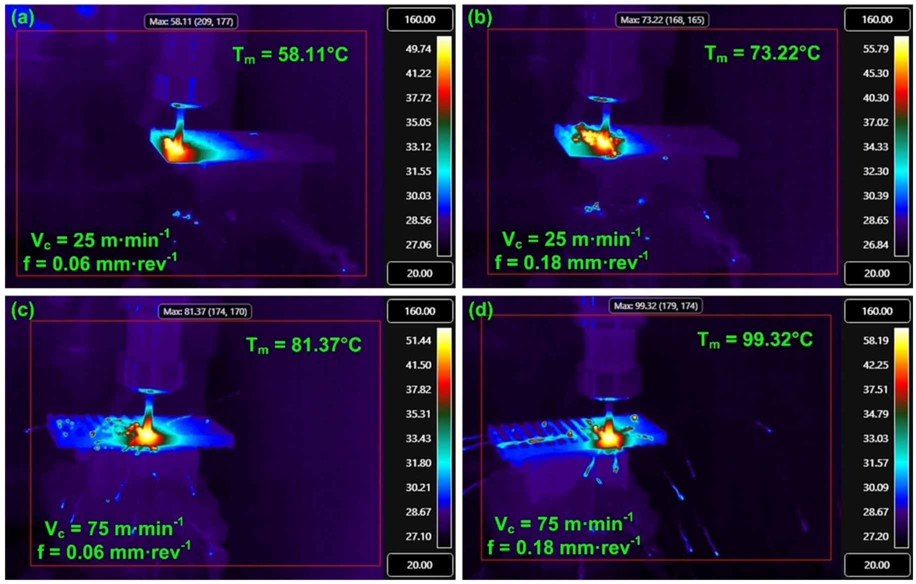

Fig. 14 Cartographies of the temperature obtained while milling heat-treated cast AlSi10Mg at a cutting speed and feed of (**a**) 25 m·min^{-1} and 0.06 mm·rev^{-1}, (**b**) 25 m·min^{-1} and 0.18 mm·rev^{-1}, (**c**) 75 m·min^{-1} and 0.06 mm·rev^{-1}, (**d**) 75 m·min^{-1} and 0.18 mm·rev^{-1}

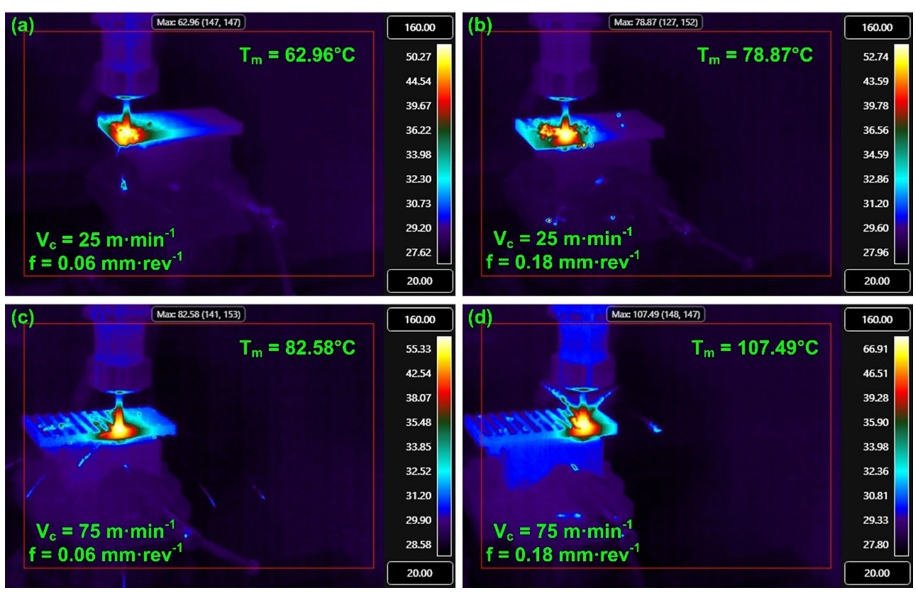

Fig. 15 Cartographies of the temperature obtained while milling heat-treated AM AlSi10Mg at a cutting speed and feed of (**a**) 25 m·min^{-1} and 0.06 mm·rev^{-1}, (**b**) 25 m·min^{-1} and 0.18 mm·rev^{-1}, (**c**) 75 m·min^{-1} and 0.06 mm·rev^{-1}, (**d**) 75 m·min^{-1} and 0.18 mm·rev^{-1}

microstructure, marked by a high concentration of grain boundaries, hinders the movement of dislocations, causing them to accumulate at these boundaries. This phenomenon enhances the yield strength and microhardness observed in AM specimens, requiring more energy for the material's plastic deformation, thereby resulting in higher machining temperatures. In contrast, the as-cast AlSi10Mg, which primarily features a microstructure composed of α-Al rich matrix, displays microhardness and yield strength [21] that are considerably lower than those of the printed material. Due to the extremely ductile behavior, the as-cast AlSi10Mg offered lower resistance to deformation during metal cutting, thus lowering the expended energy and the machining temperature.

Impact of heat treatment on maximum machining temperature is evident from the machining trials. Except for the samples machined at 25 m·min^{-1} speed and 0.06 mm·rev^{-1} feed, for all other process variable combinations, the temperatures generated while milling heat-treated cast AlSi10Mg are noted to be 7.6 ~ 19% higher than those recorded for as-cast AlSi10Mg. This increase is due to alterations in the microstructure and microhardness following heat treatment. The homogenized microstructure of heat-treated AlSi10Mg, along with the presence of Mg_2Si precipitates, serves as a barrier to plastic deformation, thereby improving microhardness and yield strength of the cast material [21, 49]. As a result, more energy is required to shear the material, leading to an increase in machining temperature. For instance, when the cutting speed is set at 25 m·min^{-1} and the feed rate is 0.06 mm·rev^{-1}, the highest machining temperature for the cast AlSi10Mg sample reaches 63.61 °C, whereas the heat-treated sample shows a slightly reduced temperature of 58.11 °C. The higher temperature is due to the more severe plastic deformation and friction encountered when milling the as-cast specimens.

In the case of as-built AlSi10Mg, a 9 ~ 14% decrease in the machining temperature is noted while milling heat-treated specimens. For AM AlSi10Mg, ultrafine microstructure, marked by high concentration of grain boundaries, hinders the movement of dislocations, leading to their accumulation at these boundaries. This effect plays a role in enhancing the yield strength and microhardness. As a result, the material displays a pronounced hardening effect during machining, expending higher energy to shearing the material, thus increasing the machining temperature. However, after heat treatment, the interconnected, fibrous coral-like Si particles are transformed into spherical particles uniformly dispersed within the Al matrix, thereby reducing dislocation pile-up at the grain boundaries. As a result, lower energy is needed to plastically deform the material, thus lowering the magnitude of the machining temperature. Additionally, the reduction in microhardness of heat-treated AlSi10Mg promotes smoother chip flow across the machining interface, which reduces friction and leads to lower machining temperatures compared to untreated AM AlSi10Mg specimens [52].

3.4.3 Surface roughness

In the study, changes in surface texture were quantitatively assessed by measuring surface roughness, considering the influence of cutting parameters only. The influence of subsurface microstructural changes and residual stress on the surface texture was not explored. Figure 16 demonstrates how cutting parameters influence surface roughness during the milling of cast and AM AlSi10Mg, both in untreated and heat-treated states. As anticipated, surface roughness increases with higher feed rates, while it diminishes with elevated cutting speeds. When feed rates are increased, the tool travels a greater distance with each revolution, leading to more widely spaced feed marks that contribute to higher surface roughness [53]. Furthermore, the relatively dull peaks seen at lower cutting feeds transform into sharper and more pronounced patterns as the feed rises, thereby increasing the width and height of surface asperities. Additionally, greater volume of material is removed in the same timeframe, requiring more energy and force to deform the material beyond its yield strength. This rise in cutting force can cause tool deflection and vibration, further deteriorating surface quality. Conversely, when cutting

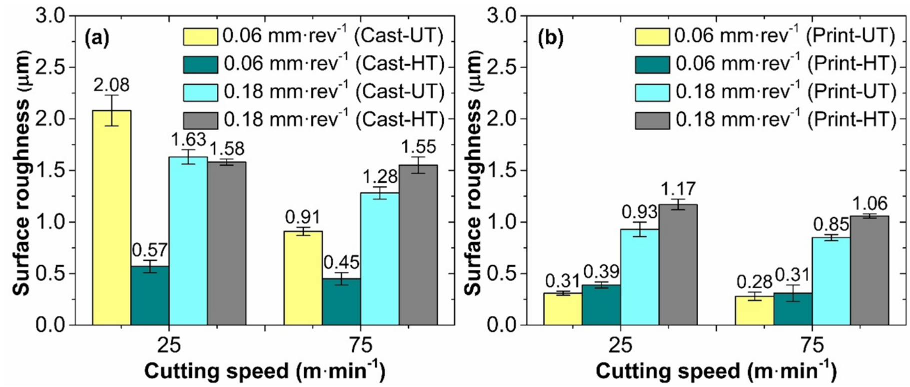

Fig. 16 Surface roughness variation with process variables for untreated and heat-treated (**a**) Cast alloy, (**b**) Printed alloy

speeds are increased, the shorter contact duration between the tool and the workpiece facilitates quicker chip removal, contributing to an improved surface finish. Additionally, elevated cutting speeds typically result in lower cutting forces, which helps minimize tool deflection and vibrations, further improving surface quality.

Moreover, material fabrication route and subsequent heat treatment significantly affect the surface roughness after machining. As-cast AlSi10Mg consistently exhibits higher surface roughness compared to its AM counterpart. Notably, under low cutting speed (25 m·min^{-1}) and feed rate (0.06 mm·rev^{-1}), the as-cast material shows a relatively poor surface finish, with a surface roughness of 2.02 μm (Fig. 17(a)). Conversely, at a higher cutting speed (75 m·min^{-1}) and feed rate (0.18 mm·rev^{-1}), a noticeable improvement is observed, with surface roughness decreasing to 1.31 μm, as shown in Fig. 17(b). The surface finish of the as-cast alloy has been notably affected by its microstructure and microhardness, especially at lower cutting feeds and speeds. As detailed in Sect. 3.1.1 and 3.1.2, as-cast AlSi10Mg primarily features a microstructure with an α-Al rich matrix, resulting in lower microhardness of 73.7 HV and reduced yield strength [21] when compared to the printed material.

Due to its highly ductile nature, the material experiences significant plastic deformation, leading to material smearing and subpar surface finish when operating at lower feeds and cutting speeds. Moreover, according to Warsi et al. [54], there exists a region called 'avoidance zones' in the metal cutting process where the machining of soft ductile material can exhibit the ploughing phenomenon during the machining operation. Such a region occurs when machining the ductile materials at lower feed and speed values. In such cases, due to the excessive plastic deformation, the machined surface shows feed marks, which are obliterated by the drag marks, resulting in a poor surface finish. Surface finish is also impacted by traces of built-up edge (BUE) adhering to the machined surface.

Compared to the as-cast material, AM AlSi10Mg demonstrates a superior surface finish. At a lower cutting speed (25 m·min^{-1}) and feed rate (0.06 mm·rev^{-1}), surface roughness of 0.33 μm is recorded (see Fig. 17(c)). Even under higher cutting conditions of 75 m·min^{-1} speed and 0.18 mm·rev^{-1} feed, surface roughness remains relatively low at 0.82 μm (see Fig. 17(d)), which is significantly better than that of as-cast material. This improved surface quality is largely attributed to the refined microstructure inherent to AM AlSi10Mg. The fine cellular dendritic structure typically formed in AM material

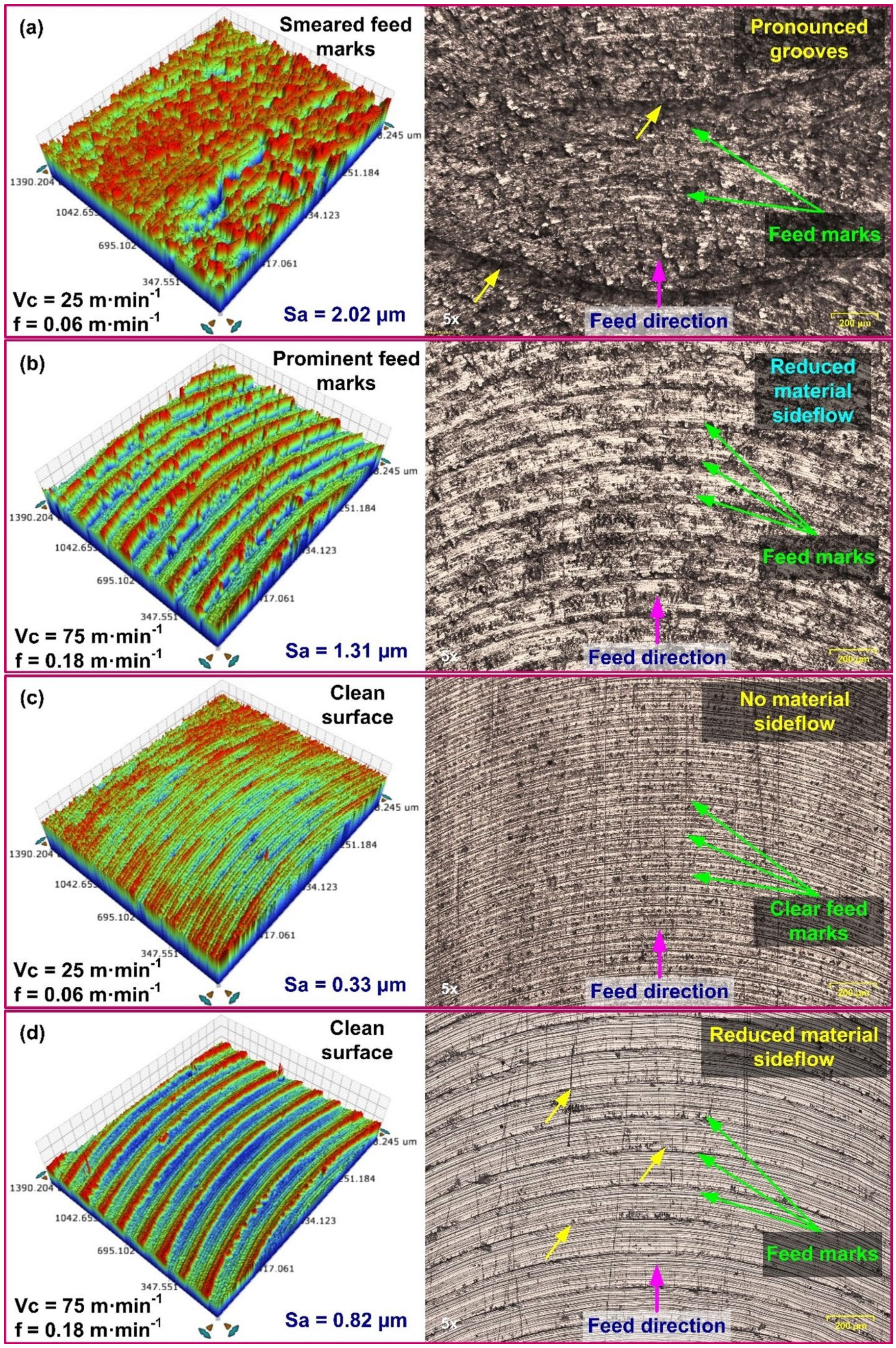

Fig. 17 3D topography and morphology of milled surfaces in (**a-b**) As-cast AlSi10Mg, (**c-d**) As-built AlSi10Mg

affects the machinability. Ultrafine microstructure, characterized by a high density of grain boundaries, impedes the movement of dislocations, causing them to accumulate at these boundaries. This effect is responsible for the enhanced yield strength and increased microhardness (146 ~ 149 HV) observed in AM specimens. During machining, the AM material exhibits a significant hardening effect, undergoing a shearing process that results in uniform feed marks and an excellent surface finish, even at lower feed and speed settings.

Effect of heat treatment on surface roughness was assessed for both cast and AM AlSi10Mg. After undergoing heat treatment, the cast AlSi10Mg exhibited a significant improvement in surface finish. Specifically, when machined at a speed of 25 m·min^{-1} and a feed of 0.06 mm·rev^{-1}, surface roughness decreased to 0.62 µm (refer to Fig. 18(a)). Under higher cutting conditions of 75 m·min^{-1} speed and 0.18 mm·rev^{-1} feed, surface roughness of 1.65 µm was recorded (see Fig. 18(b)). In comparison to the as-cast samples, this signifies a decrease in surface roughness ranging from 20% to 69%. The

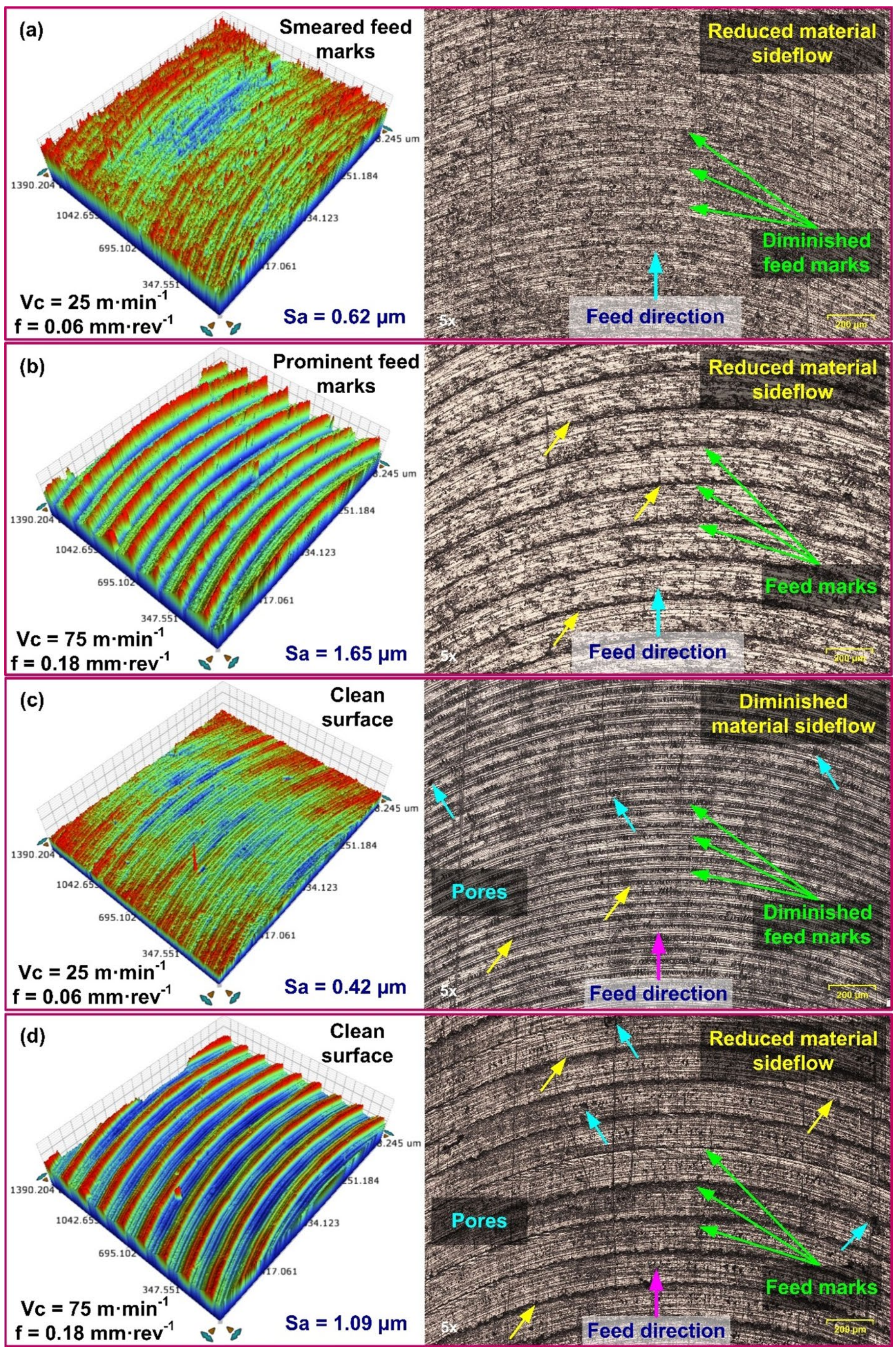

Fig. 18 3D topography and morphology of milled surfaces in heat-treated (**a-b**) Cast AlSi10Mg, (**c-d**) Printed AlSi10Mg

enhancement is mainly due to microstructural and microhardness changes induced by the heat treatment.

As outlined in Sect. 3.2, the needle-like Si lamellae with irregularly faceted shapes transform into more spherical and separated particles, thereby homogenizing the microstructure of AlSi10Mg during heat treatment. Furthermore, the Mg_2Si precipitates within the material impede plastic deformation, leading to an increase in microhardness (127.4 HV) and yield strength of cast alloy [21, 47]. The morphology and topography reveal distinct feed marks without any smear marks, signifying a clear shift in material removal mechanism from ploughing to shearing. Additionally, presence of hard phases reduces the ductility, encouraging chip brittleness and breakage, which subsequently improves the surface finish.

However, surface roughness increases when milling heat-treated AM AlSi10Mg. At a cutting speed of 25 m·min^{-1} and a feed of 0.06 mm·rev^{-1}, heat-treated AM samples show an average surface roughness of 0.42 µm, as illustrated in Fig. 18(c). If cutting speed is raised to 75 m·min^{-1} and the feed rate to 0.18 mm·rev^{-1}, the surface roughness rises to 1.09 µm, as depicted in Fig. 18(d). This indicates a 21–25% increase in surface roughness after heat treatment compared to as-built AlSi10Mg. This change is attributed to fragmentation and spheroidization of the coral-like fibrous Si structures in the AM AlSi10Mg [7, 21]. As eutectic network breaks down, the material experiences a reduction in both elastic modulus and yield strength [11]. Also, the microstructure coarsening lowers the microhardness (82.6 ~ 84.9 HV) and enhances the ductility of AlSi10Mg. Consequently, the lateral flow of material increases, leading to greater surface roughness in the heat-treated AM specimen.

3.4.4 Chip morphology

The chips generated during machining can reveal the material's machinability and offer important insights into cutting force, specific cutting energy, tool wear, and surface finish. It can also help determine the optimal machining conditions, which can ensure a stable and efficient cutting process. Figure 19 illustrates the chip morphologies obtained during the milling process of cast AlSi10Mg, both in its original as-cast state and after undergoing heat treatment. A difference in the chip morphology is observed for similar cutting conditions based on the material type (fabrication route) and heat treatment. As-cast AlSi10Mg produces very long and continuous chips with signs of material adhesion (see Fig. 19(a), indicating the formation of BUE at the cutting edge of the tool, as shown in Fig. 20 (a, b). The generation of long, continuous chips is attributed to the lower hardness and higher ductility exhibited by the as-cast material. Due to the ductile nature of the material, the material underwent ploughing, resulting in material smearing and BUE formation, thereby deteriorating the surface finish. However, the chips formed while milling AM AlSi10Mg are fragmented and curly, as shown in Fig. 19(b). Higher hardness of AM AlSi10Mg contributed to the brittle behavior of the material, resulting in chip fragmentation. As a result, AM material produces a very good surface finish without any BUE formation.

Moreover, the chip morphology of cast AlSi10Mg is significantly affected by heat treatment. As shown in Fig. 19(c), there is a clear decrease in chip length in heat-treated cast AlSi10Mg. The T6 heat treatment process improves the microstructure and increases hardness by ensuring a more even distribution of Si. This enhanced the

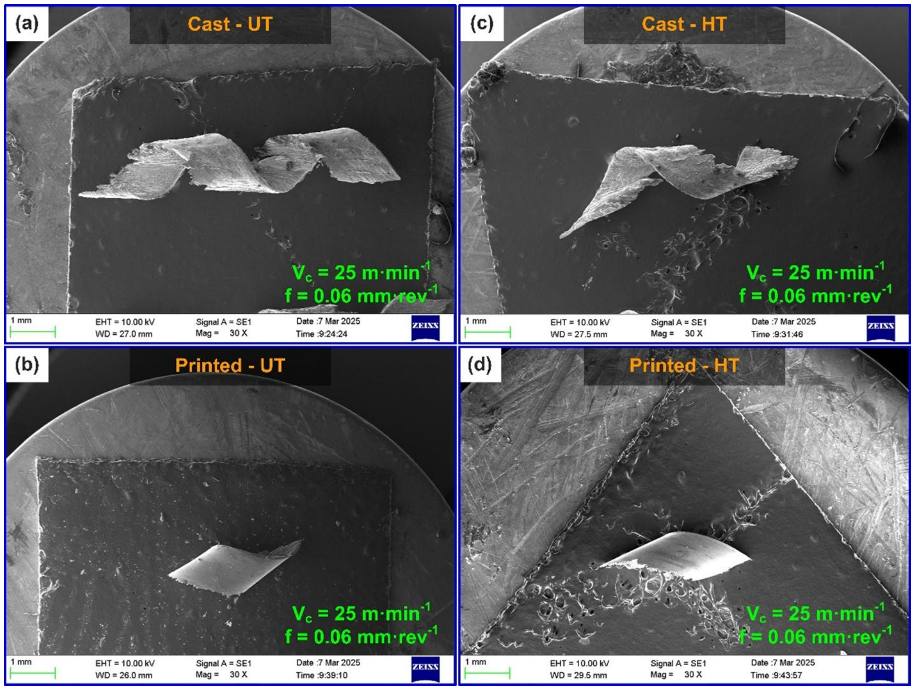

Fig. 19 Morphology of chip obtained while milling (**a**) As-cast AlSi10Mg, (**b**) As-built AlSi10Mg, (**c**) Heat-treated cast AlSi10Mg, (**d**) Heat-treated printed AlSi10Mg

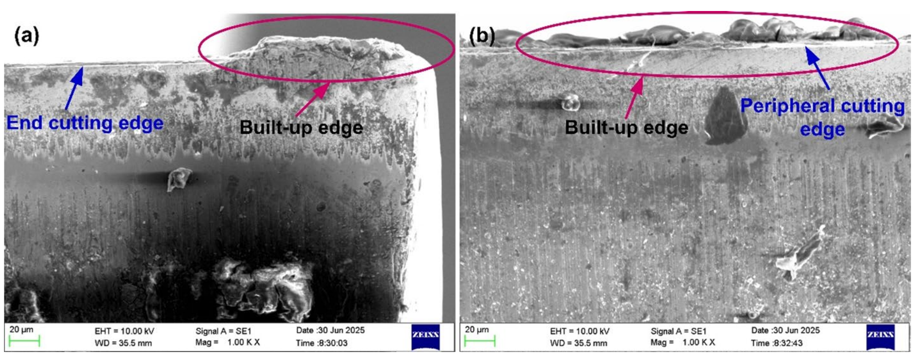

Fig. 20 Built-up edge (BUE) observed at the (**a**) End cutting edge, (**b**) Peripheral cutting edge of the end mill while milling as-cast alloy

chip embrittlement and breakability, reducing the size and length of the chips produced. Additionally, a significant reduction in chip adhesion and BUE is observed. Consequently, the surface finish of T6 heat-treated AlSi10Mg is superior to that of as-cast material under similar cutting conditions. Figure 19(d) shows the chip produced while milling AM AlSi10Mg subjected to heat treatment. In case of AM AlSi10Mg, heat treatment has a negligible effect on the chip morphology. The chips produced while milling as-built AlSi10Mg are comparable in size and length to the chips produced when milling heat-treated AlSi10Mg. Heat treatment eliminated lattice defects and increased grain size in AM AlSi10Mg, thereby enhancing its ductility. However, this had a negligible influence on the chip size. Overall, it can be noted that the chip morphology is dependent on material fabrication route and the heat treatment cycle to which the material is subjected.

4 Conclusions

This research explored microstructure, microhardness, and machinability of cast and additively manufactured AlSi10Mg, as well as impact of T6 heat treatment on these responses. Results are summarized as follows.

- The as-cast AlSi10Mg exhibited a microstructure consisting of dendritic primary α-Al and a lamellar eutectic structure made up of α-Al and Si. In contrast, the AM material showed a refined cellular dendritic structure with a fibrous network of eutectic Si defining the cell walls.
- In both cast and AM AlSi10Mg materials, due to T6 heat treatment, the Si underwent fragmentation due to the heat treatment, followed by spheroidization and coarsening. Nevertheless, the Si particles in the heat-treated AM AlSi10Mg were more refined and exhibited greater spheroidization compared to those in the cast version, indicating a significant influence of the solution treatment and aging time on spheroidization and coarsening.
- The AM material exhibited a hardness ranging from 142 to 146 HV, which was greater than that of the as-cast material, measured at 74 HV. Nonetheless, heat treatment significantly increased the hardness of the cast material, resulting in a 73% rise compared to the untreated version. In contrast, the AM material experienced a reduction in hardness by 71 to 73% following heat treatment. This variation in microhardness is linked to the microstructural changes that occur in both the cast and AM AlSi10Mg after undergoing heat treatment.
- The cutting force recorded while milling as-built AM material was 81 to160% higher than its as-cast counterpart. However, after heat treatment, the cutting force for cast material increased by 28–60% as compared to the as-cast state. In the case of the AM material, a 14 to 62% reduction in the cutting force was noted when milling the heat-treated AM material.
- The maximum machining temperature observed during milling of the AM material was 9–48% higher than that of the cast material. Following heat treatment, changes in microstructure and microhardness led to a 7.6–19% increase in machining temperature for cast AlSi10Mg. In contrast, the heat-treated AM material showed a 9–14% reduction in machining temperature compared to as-built material.
- The highest surface roughness was found when machining as-cast material, whereas a superior surface finish was noted in untreated AM material. Under identical machining conditions, surface roughness of the as-cast material was between 50% and 551% greater than that of as-built AM material. However, after heat treatment, surface roughness of cast material decreased by 32–264%, whereas the AM material exhibited a 10–26% increase in surface roughness compared to as-built material.
- Longer chips were observed when milling cast specimens, while shorter chips were generated when milling the AM material. Heat treatment reduced chip size for the cast material, whereas no significant change was observed in the AM material.

Acknowledgements
The authors would like to acknowledge Manipal Academy of Higher Education, Manipal, for providing the facilities for conducting research. We sincerely thank Oerlikon Balzers Coating India Private Limited for helping with the tool coating. We also thank the Department of Mechanical Engineering, Indian Institute of Technology Tirupati, for providing access to the 3D non-contact profilometer and the data.

Author contributions

Conceptualization: GB, NK, RS; Methodology: NK, RS; Investigation, Visualization, Data Acquisition: AKV, SRU; Formal Analysis: AKV, NK, GB; Writing-Original Draft Preparation: AKV, GB, RS; Validation: AKV, SRU; Writing-Review and Editing: AP, SRU; Supervision: GB.

Funding

Open access funding provided by Manipal Academy of Higher Education, Manipal. This research did not receive any specific grant from funding agencies in the public, commercial, or not-for-profit sectors.

Data availability

Data included in the article/supplementary material is referenced in the article.

Declarations

Ethics approval and consent to participate

Not applicable.

Consent for publication

Not applicable.

Competing interests

The authors declare no competing interests.

Received: 17 December 2025 / Accepted: 20 May 2026

Published online: 26 May 2026

References

1. Edwards P, Ramulu M. Fatigue performance evaluation of selective laser melted Ti–6Al–4V. Mater Sci Eng A. 2014;598:327–37. https://doi.org/10.1016/j.msea.2014.01.041.
2. Sames WJ, List FA, Pannala S, Dehoff RR, Babu SS. The metallurgy and processing science of metal additive manufacturing. Int Mater Rev. 2016;61:315–60. https://doi.org/10.1080/09506608.2015.111664.
3. Bose S, Ke D, Sahasrabudhe H, Bandyopadhyay A. Additive manufacturing of biomaterials. Prog Mater Sci. 2018;93:45–111. https://doi.org/10.1016/j.pmatsci.2017.08.003.
4. Zakay A, Aghion E. Effect of post-heat treatment on the corrosion behavior of AlSi10Mg alloy produced by additive manufacturing. J Mineral Metal Mater Soc. 2019;71:1150–7. https://doi.org/10.1007/s11837-018-3298-x.
5. Wei P, Chen Z, Zhang S, Fang X, Lu B, Zhang L, Wei Z. Effect of T6 Heat Treatment on the Surface Tribological and Corrosion Properties of AlSi10Mg Samples Produced by Selective Laser Melting. Mater Charact. 2021;171:110769. https://doi.org/10.1016/j.matchar.2020.110769.
6. Iturrioz A, Gil E, Petite MM, Garciandia F, Mancisidor AM, San Sebastian M. Selective laser melting of AlSi10Mg alloy: influence of heat treatment condition on mechanical properties and microstructure. Weld World. 2018;62:885–92. https://doi.org/10.1007/s40194-018-0592-8.
7. Zhou L, Mehta A, Schulz E, McWilliams B, Cho K, Sohn Y. Microstructure, precipitates and hardness of selectively laser melted AlSi10Mg alloy before and after heat treatment. Mater Charact. 2018;143:5–17. https://doi.org/10.1016/j.matchar.2018.04.022.
8. Kempf A, Hilgenberg K. Influence of heat treatments on AlSi10Mg specimens manufactured with different laser powder bed fusion machines. Mater Sci Eng A. 2021;818:141371. https://doi.org/10.1016/j.msea.2021.141371.
9. Hadadzadeh A, Amirkhiz BS, Mohammadi M. Contribution of Mg_2Si precipitates to the strength of direct metal laser sintered AlSi10Mg. Mater Sci Eng A. 2019;739:295–300. https://doi.org/10.1016/j.msea.2018.10.055.
10. Arun K, Ramu M, Kota PK. Studies on mechanical and corrosion behaviour of heat-treated AlSi10Mg alloy fabricated by PBF-LM. Prog Addit Manuf. 2024;9:1061–70. https://doi.org/10.1007/s40964-023-00503-x.
11. Li W, Li S, Liu J, Zhang A, Zhou Y, Wei Q, Yan C, Shi Y. Effect of heat treatment on AlSi10Mg alloy fabricated by selective laser melting: Microstructure evolution, mechanical properties and fracture mechanism. Mater Sci Eng A. 2016;663:116–25. https://doi.org/10.1016/j.msea.2016.03.088.
12. Maleki E, Bagherifard S, Unal O, Guagliano M. Hybrid Intelligence approach to study post-processing impact on the mechanical performance of notched additively manufactured AlSi10Mg. Mater Des. 2024;248:113462. https://doi.org/10.1016/j.matdes.2024.113462.
13. Kok Y, Tan XP, Wang P, Nai MLS, Loh NH, Liu E, Tor SB. Anisotropy and Heterogeneity of Microstructure and Mechanical Properties in Metal Additive Manufacturing: A Critical Review. Mater Des. 2018;139:565–86. https://doi.org/10.1016/j.matdes.2017.11.021.
14. Di Giovanni MT, de Menezes JTO, Bolelli E, Cerri G, Castrodeza EM. Fatigue crack growth behavior of a selective laser melted AlSi10Mg. Eng Fract Mech. 2019;217:106564. https://doi.org/10.1016/j.engfracmech.2019.106564.
15. Yan Q, Song B, Shi Y. Comparative study of performance comparison of AlSi10Mg alloy prepared by selective laser melting and casting. J Mater Sci Technol. 2020;41:199–208. https://doi.org/10.1016/j.jmst.2019.08.049.
16. Razavi N, Bagherifard S, Hafnor S, Spiller S, Guagliano M, Berto F. Fatigue analysis of as-built and heat-treated severely notched AlSi10Mg alloy specimens made by laser powder bed fusion technology. Int J Fatigue. 2024;179:108041. https://doi.org/10.1016/j.ijfatigue.2023.108041.
17. Wang LF, Sun J, Yu XL, Shi Y, Zhu XG, Cheng LY, Liang HH, Yan B, Guo LJ. Enhancement in mechanical properties of selectively laser-melted AlSi10Mg aluminum alloys by T6-like heat treatment. Mater Sci Eng A. 2018;734:299–310. https://doi.org/10.1016/j.msea.2018.07.103.

18. Aboulkhair NT, Maskery I, Tuck C, Ashcroft I, Everitt NM. The microstructure and mechanical properties of selectively laser melted AlSi10Mg: the effect of a conventional T6-like heat treatment. Mater Sci Eng A. 2016;667:139–46. https://doi.org/10.1016/j.msea.2016.04.092.
19. Girelli L, Tocci Gelfi MM, Pola A. Study of heat treatment parameters for additively manufactured AlSi10Mg in comparison with corresponding cast alloy. Mater Sci Eng A. 2019;739:317–28. https://doi.org/10.1016/j.msea.2018.10.026.
20. Tonolini P, Montesano L, Tocci M, Pola A, Gelfi M. Wear behavior of AlSi10Mg alloy produced by laser-based powder bed fusion and gravity casting. Adv Eng Mater. 2021;23:2100147. https://doi.org/10.1002/adem.202100147.
21. Aboulkhair NT, Tuck C, Ashcroft I, Maskery I, Everitt NM. On the precipitation hardening of selective laser melted AlSi10Mg. Metall Mater Trans A. 2015;46:3337–41. https://doi.org/10.1007/s11661-015-2980-7.
22. Shakil SI, Hadadzadeh A, Amirkhiz BS, Pirgazi H, Mohammadi M, Haghshenas M. Additive manufactured versus cast AlSi10Mg alloy: Microstructure and micromechanics. Results Mater. 2021;10:100178. https://doi.org/10.1016/j.rinma.2021.100178.
23. Charan BS, Srikanth M, Swamy S, Ravi KR, Pattanayak DK. Analysis of phase, microstructure, and mechanical characteristics of selective laser melted AlSi10Mg alloy after post-heat treatment. Prog Addit Manuf. 2025;10:593–604. https://doi.org/10.1007/s40964-024-00643-8.
24. Park TH, Baek MS, Hyer H, Sohn Y, Lee KA. Effect of direct aging on the microstructure and tensile properties of AlSi10Mg alloy manufactured by selective laser melting process. Mater Charact. 2021;176:111113. https://doi.org/10.1016/j.matchar.2021.111113.
25. Ibrahim M, Abdelaziz M, Samuel A, Doty H, Samuel F. Spheroidization and Coarsening of Eutectic Si Particles in Al-Si-Based Alloys. Adv Mater Sci Eng. 2021;2021:6678280. https://doi.org/10.1155/2021/6678280.
26. Wang C, He D, He C, Han F, Li J, Cui L. Effect of heat treatments on microstructure and mechanical behavior of laser welded LPBF AlSi10Mg alloys. Mater Today Commun. 2024;38:108478. https://doi.org/10.1016/j.mtcomm.2024.108478.
27. Brandl E, Heckenberger U, Holzinger V, Buchbinder D. Additive manufactured AlSi10Mg samples using Selective Laser Melting (SLM): microstructure, high cycle fatigue, and fracture behavior. Mater Des. 2012;34:159–69. https://doi.org/10.1016/j.matdes.2011.07.067.
28. Casati R, Nasab MH, Coduri M, Tirelli V, Vedani M. Effects of platform preheating and thermal-treatment strategies on properties of AlSi10Mg alloy processed by selective laser melting. Metals. 2018;8:954. https://doi.org/10.3390/met8110954.
29. Kan WH, Nadot Y, Foley M, Ridosz L, Proust G, Cairney JM. Factors that affect the properties of additively-manufactured AlSi10Mg: porosity versus microstructure. Addit Manuf. 2019;29:100805. https://doi.org/10.1016/j.addma.2019.100805.
30. Dong D, Wu Q, Jiang A, Li Y, Qin Y, Ma S, Zheng H. Effect of substrate preheating on microstructure and mechanical properties of AlSi10Mg alloy manufactured by laser powder bed fusion. Mater Lett. 2026;405:139740. https://doi.org/10.1016/j.matlet.2025.139740.
31. Zimmermann M, Müller D, Kirsch B, Greco S, Aurich JC. Analysis of the machinability when milling AlSi10Mg additively manufactured via laser-based powder bed fusion. Int J Adv Manuf Technol. 2021;112:989–1005. https://doi.org/10.1007/s00170-020-06391-7.
32. Struzikiewicz G, Sioma A. Surface Topographic Features after Milling of Additively Manufactured AlSi10Mg Aluminum Alloy. Mater. 2022;15:3604. https://doi.org/10.3390/ma15103604.
33. Randolph O, Kazi A, Lin TT, Zvanut R, Tai BL. Single point machining of A205 aluminum: A comparison of cast and additively manufactured materials. J Manuf Process. 2024a;110:252–62. https://doi.org/10.1016/j.jmapro.2023.12.045.
34. Randolph O, Zvanut R, Tai BL. Microstructure analysis and machinability of additively manufactured A205 aluminum with heat treatments. J Manuf Process. 2024b;127:51–61. https://doi.org/10.1016/j.jmapro.2024.07.111.
35. Ramoni M, Shanmugam R, Ross NS, Gupta MK. An experimental investigation of hybrid manufactured SLM based Al-Si10-Mg alloy under mist cooling conditions. J Manuf Process. 2021;70:225–35. https://doi.org/10.1016/j.jmapro.2021.08.045.
36. Ross NS, Ananth MBJ, Jafferson JM, Rajeshkumar L, Kumar MS. Performance assessment of vegetable oil–based MQL in milling of additively manufactured AlSi10Mg for sustainable production. Biomass Convers Biorefin. 2024;14:8693–710. https://doi.org/10.1007/s13399-022-02967-3.
37. Ross NS, Srinivasan N, Belsam Jeba Ananth M, AlFaify AY, Anwar S, Gupta MK. Performance assessment of different cooling conditions in improving the machining and tribological characteristics of additively manufactured AlSi10Mg alloy. Tribol Int. 2023;186:108631. https://doi.org/10.1016/j.triboint.2023.108631.
38. Al-Rubaie KS, Melotti S, Rabelo A, Paiva JM, Elbestawi MA, Veldhuis SC. Machinability of SLM-produced Ti6Al4V. J Manuf Process. 2020;57:768–86. https://doi.org/10.1016/j.jmapro.2020.07.035.
39. Xu S, Lu Q, Ou Y, Zhang P, Yan H, Sun T, Tian Y. Effect of heat treatment on the anisotropic mechanical properties of AlSi10Mg fabricated by selective laser melting. J Mater Eng Perform. 2024;33:10401–14. https://doi.org/10.1007/s11665-023-08669-9.
40. Maamoun AH, Elbestawi M, Dosbaeva GK, Veldhuis SC. Thermal post-processing of AlSi10Mg parts produced by Selective Laser Melting using recycled powder. Addit Manuf. 2018;21:234–47. https://doi.org/10.1016/j.addma.2018.03.014.
41. Li XP, Wang XJ, Saunders M, Suvorova A, Zhang LC, Liu YJ, Fang MH, Huang ZH, Sercombe TB. A selective laser melting and solution heat treatment refined Al–12Si alloy with a controllable ultrafine eutectic microstructure and 25% tensile ductility. Acta Mater. 2015;95:74–82. https://doi.org/10.1016/j.actamat.2015.05.017.
42. Fathi P, Mohammadi M, Duan X, Nasiri AM. A comparative study on corrosion and microstructure of direct metal laser sintered AlSi10Mg_200C and die cast A360.1 aluminum. J Mater Proc Technol. 2018;259:1–14. https://doi.org/10.1016/j.jmatprotec.2018.04.013.
43. Bisht MS, Gaur V, Singh IV. On mechanical properties of SLM Al–Si alloy: Role of heat treatment-induced evolution of silicon morphology. Mater Sci Eng A. 2022;858:144157. https://doi.org/10.1016/j.msea.2016.03.088.
44. Alghamdi F, Song X, Hadadzadeh A, Shalchi-Amirkhiz B, Mohammadi M, Haghshenas M. Post heat treatment of additive manufactured AlSi10Mg: On silicon morphology, texture and small-scale properties. Mater Sci Eng A. 2020;783:139296. https://doi.org/10.1016/j.msea.2020.139296.
45. Seifeddine S, Johansson S, Svensson IL. The influence of cooling rate and manganese content on the β-Al5FeSi phase formation and mechanical properties of Al–Si-based alloys. Mater Sci Eng A. 2008;490:385–90. https://doi.org/10.1016/j.msea.2008.01.056.

46. Pourkhorshid E, Rometsch P, Bois-Brochu A, Taylor A, Marceau RK, Chen XG. Effect of Mn on microstructural characteristics and mechanical behavior of AlSi10Mg alloys produced by laser powder bed fusion. Addit Manuf. 2025;110:104923. https://doi.org/10.1016/j.addma.2025.104923.
47. Meng G, Gong Y, Zhang J, Ren Q, Zhao J. Microstructure effect on the machinability behavior of additive and conventionally manufactured Inconel 718 alloys. J Mater Proc Technol. 2024;324:118228. https://doi.org/10.1016/j.jmatprotec.2023.118228.
48. Kolomy S, Maly M, Sedlak J, Zouhar J, Slany M, Hrabec P, Kouril K. Machinability of extruded H13 tool steel: Effect of cutting parameters on cutting forces, surface roughness, microstructure, and residual stresses. Alex Eng J. 2024;99:394–407. https://doi.org/10.1016/j.aej.2024.05.018.
49. Beder M, Akçay SB, Varol T, Çuvalcı H. The effect of heat treatment on the mechanical properties and oxidation resistance of AlSi10Mg alloy. Arab J Sci Eng. 2024;49:15335–46. https://doi.org/10.1007/s13369-024-08971-1.
50. Sun Y, Sun J, Li J, Xiong Q. An experimental investigation of the influence of cutting parameters on cutting temperature in milling Ti6Al4V by applying semi-artificial thermocouple. Int J Adv Manuf Technol. 2014;70:765–73. https://doi.org/10.1007/s00170-013-5294-1.
51. Koklu U, Çoban H. Effect of dipped cryogenic approach on thrust force, temperature, tool wear and chip formation in drilling of AZ31 magnesium alloy. J Mater Res Technol. 2020;9:2870–80. https://doi.org/10.1016/j.jmrt.2020.01.038.
52. Joshy J, George A, Kuriachen B, Mathew J. Influence of post processing on the micro-machinability of selective laser melted AlSi10Mg: an experimental investigation. Mater Manuf Proc. 2023;38:516–28. https://doi.org/10.1080/10426914.2022.2075886.
53. Kolomy S, Maly M, Doubrava M, Sedlak J, Zouhar J, Cupera J. Effect of microstructure on machinability of extruded and conventional H13 tool steel. Mater Des. 2025;254:114132. https://doi.org/10.1016/j.matdes.2025.114132.
54. Warsi SS, Ahmad R, Jaffery SHI, Agha MH, Khan M. Development of specific cutting energy map for sustainable turning: A study of Al 6061 T6 from conventional to high cutting speeds. Int J Adv Manuf Technol. 2020;106:2949–60. https://doi.org/10.1007/s00170-019-04836-2.

Publisher's note